

# Morphogenesis and proportionate growth: A finite element investigation of surface growth with coupled diffusion

Virginia von Streng<sup>a,b</sup>, Rami Abi-Akl<sup>c</sup>, Bianca Giovanardi<sup>d</sup>, Tal Cohen<sup>c,b,\*</sup>

<sup>a</sup>*Department of Mechanical and Process Engineering, ETH Zurich, Switzerland*

<sup>b</sup>*Department of Civil and Environmental Engineering, Massachusetts Institute of Technology, Cambridge, MA 02139*

<sup>c</sup>*Department of Mechanical Engineering, Massachusetts Institute of Technology, Cambridge, MA 02139*

<sup>d</sup>*Department of Aeronautics and Astronautics, Massachusetts Institute of Technology, Cambridge, MA 02139*

---

## Abstract

Modeling the spontaneous evolution of morphology in natural systems and its preservation by proportionate growth remains a major scientific challenge. Yet, it is conceivable that if the basic mechanisms of growth and the coupled kinetic laws that orchestrate their function are accounted for, a minimal theoretical model may exhibit similar growth behaviors. The ubiquity of surface growth, a mechanism by which material is added or removed on the boundaries of the body, has motivated the development of theoretical models, which can capture the diffusion-coupled kinetics that govern it. However, due to their complexity, application of these models has been limited to simplified geometries. In this paper, we tackle these complexities by developing a finite element framework to study the diffusion-coupled growth and morphogenesis of finite bodies formed on uniform and flat substrates. We find that in this simplified growth setting, the evolving body exhibits a sequence of distinct growth stages that are reminiscent of natural systems, and appear spontaneously without any externally imposed regulation or coordination. The computational framework developed in this work can serve as the basis for future models that are able to account for growth in arbitrary geometrical settings, and can shed light on the basic physical laws that orchestrate growth and morphogenesis in the natural world.

---

## 1. Introduction

From the life cycle of a living organism to that of an engineered artifact, the evolution of material systems is driven by competing processes of growth and decay. When these processes are coupled to simultaneously occurring adaptations, such as accumulation of mechanical stresses, deformation, diffusion, and chemical reactions, predicting the evolution of the material system becomes a nontrivial task. In the animal kingdom, these growth processes are often described as either morphogenesis (Turing, 1952; Cross and Hohenberg, 1993), or proportionate growth (Sadhu and Dhar, 2012; Bischofberger and Nagel, 2016). The former refers to changes in shape of an evolving body, such as the breakage of symmetry in an embryo<sup>1</sup>, and the latter to changes in size that preserve the overall shape, such as the growth of a child into an adult. From the biological viewpoint, the orchestration of these complex growth processes is encoded in the DNA (Johnson and Tabin, 1997; Metzger and Krasnow, 1999).

---

\*Corresponding author.

*Email address:* talco@mit.edu (Tal Cohen)

<sup>1</sup>An embryo is initially spherical in its blastula stage.

Nonetheless, in recent years mechanics has emerged as a key player in driving natural growth (Savin et al., 2011; Tallinen et al., 2016; Budday et al., 2014), thus potentially providing a link between the biological growth factors and the physical growth process, and in turn providing basic understanding that can guide the development of intelligent fabrication technologies that mimic natural growth.

In this work, we focus our attention on material systems that can grow or degrade by reactions that occur on the boundaries of the body (i.e. surface growth) while accounting for the influence of diffusion through the bulk of the body that is needed to ‘feed’ the growth, and the resulting development of mechanical stresses. Despite the ubiquity of their manifestations that range from examples of growth and morphogenesis in nature (Thompson, 1917) and to a multitude of engineering applications, these growth processes remain poorly understood. In nature, actin gel in eukaryotic cells grows by persistent polymerization that pushes against the cell membrane (Noireaux et al., 2000; Tomassetti et al., 2016). This surface growth mechanism is also responsible for cell motility (Mogilner and Oster, 1996, 2003). Recent studies have shown that the rate of degradation of biopolymer particles in the oceans is mediated by mechanical stresses (Abi-Akl et al., 2019b; Cordero and Stocker, 2017). Addition of layers underneath the bark of a tree and the growth of sea shells and horns serve as additional examples (Skalak et al., 1997, 1982; Moulton et al., 2012). In engineering, examples range from the formation of a solid electrolyte interface that limits battery life (Horstmann et al., 2018), to drug delivery systems (Slaughter et al., 2009; Li and Mooney, 2016), and emerging fabrication techniques induced by frontal polymerization (Robertson et al., 2018; Goli et al., 2019).

In all of the examples mentioned above, the interaction between a solid backbone (e.g. a polymer network) and a diffusing fluid (e.g. a solvent) affects the rates of growth and degradation. The theoretical representation in the bulk must therefore account for both species (as in Hong et al. (2008); Chester and Anand (2010); Duda et al. (2010); Stracuzzi et al. (2018)), and the representation on the boundaries of the body should allow for chemical reactions between them, while obeying mass conservation requirements. Using this approach, Abi-Akl et al. (2019a) presented a general continuum framework for modeling the kinetics of surface growth with coupled diffusion. Various alternative approaches to modeling surface growth have been proposed (DiCarlo, 2005; Ciarletta et al., 2013; Holland et al., 2013; Papastavrou et al., 2013a; Swain and Gupta, 2018; Skalak et al., 1982, 1997; Menzel and Kuhl, 2012; Moulton et al., 2012; Tomassetti et al., 2016; Ganghoffer and Goda, 2018; Sozio and Yavari, 2017; Abeyaratne et al., 2020; Ateshian, 2007) and are reviewed in more detail by Abi-Akl et al. (2019a).

Recently, Sozio and Yavari (2019) presented a geometric theory that captures the nonlinear mechanics and incompatibilities induced by accretion, and studied various growth scenarios for given vector fields of the growth velocity. Using a different approach, Zurlo and Truskinovsky (2017, 2018) study different methods for controlling the accretion process and the resulting non-Euclidean bodies that form. In contrast, the theoretical formulation in the present work does not prescribe the kinematics of growth. Instead, it employs a kinetic law that relates between the growth velocity and its thermodynamic conjugate: the driving force of growth. The thermodynamically consistent form of the kinetic law is then chosen in accord with the specific mechanism of accretion.

To study the chemo-mechanically coupled growth process, Abi-Akl et al. (2019a) specialized the general model to a specific initial-boundary value problem of uniaxial growth. It was shown that although two separate time scales appear in the formulation (i.e. the diffusion time scale, and the growth time scale), the system rapidly adapts through a diffusion dominated response to arrive at a ‘universal path’ that is independent of initial conditions; as it evolves along this path, growth and diffusion act harmoniously. The specific growth patterns considered in earlier work (Abi-Akl et al., 2019a; Abi-Akl and Cohen, 2020) can be described by a single spatial coordinate and were thus amenable to both

analytical and numerical investigation (using a finite difference scheme). To account for more complex geometries, in this paper we develop a finite-element model. We restrict our attention to 2D growth settings (i.e. generalized plane-strain) and take advantage of our *a priori* knowledge on the existence of a ‘universal growth path’, to reduce the complexity of the numerical simulation.

The developed model decouples the growth process into diffusion-deformation and growth steps. Every diffusion-deformation step is solved as a boundary value problem in quasi-equilibrium. Applying the growth velocities resulting from the diffusion-deformation solution to the material domain leads to a new material geometry, which then is remeshed. Subsequently, the next diffusion-deformation problem is solved on the new mesh. A simplified approach for adding material on a flat rigid growth surface is shown to ease the computation by neglecting the development of residual stresses due to differential growth along the association surface. It is then confirmed that this effect is negligible in the considered growth settings.

The paper is organized as follows: in Section 2, we define the problem setting and briefly recapitulate the governing equations that were developed by Abi-Akl et al. (2019a). Then, in Section 3, we discuss the numerical solution of the highly nonlinear and coupled system of equations while highlighting the procedure to capture the time evolution of the domain. The results of three representative simulations are presented in Section 4. Following validation of the model against analytical results for the 1D case, growth of more general 2D systems with varying boundary conditions are portrayed, and the distinct stages of growth that emerge in these systems are discussed. Finally, we provide concluding remarks in Section 5.

## 2. Problem setting and governing equations

Consider a rigid and flat substrate submersed in a solvent. A chemical reaction that can occur on this substrate promotes the formation of new solid material. As accretion progresses, a mixed species continuum body is formed. We consider each species to be separately incompressible and distinguish between the current configuration of the body  $\mathcal{B}$ , which occupies the region  $\mathcal{R}(t)$  in the physical space, and its solvent free (i.e. dry) image  $\mathcal{R}^R(t)$  in the reference space<sup>2</sup>. Each material point that is attached to the body in the reference configuration, denoted by  $\mathbf{X}$ , sustains its location throughout the growth process, and its mapping to  $\mathcal{R}(t)$  is denoted by  $\mathbf{x}(\mathbf{X}, t)$ .

Previous studies have shown that, due to build up of residual stresses, description of the natural reference configuration of the grown body may require a higher dimensional reference space (Abi-Akl et al., 2019a; Tomassetti et al., 2016). In this work we bypass this complexity by focusing our attention on flat substrates and making a simplifying assumption on the growth process (as described in detail in Section 3.3). It will be shown that for the considered geometric setting and constitutive model, the effects that are omitted due to this simplification are negligible. Hence, this approach can be extended in the future for arbitrary growth surfaces.

---

<sup>2</sup>From hereon, quantities in the reference space are denoted by the superscript  $(\cdot)^R$ .

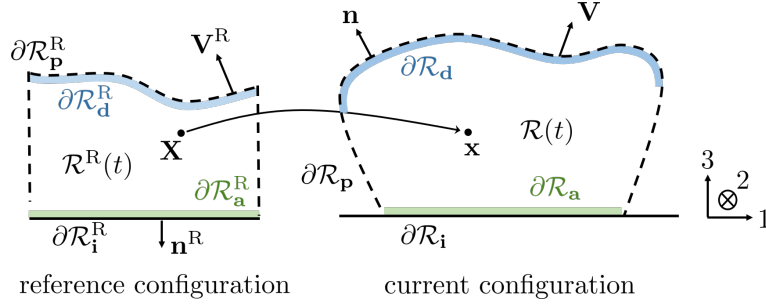


Figure 1: Illustration of the grown body in both current and reference configurations. Different regions of the boundary are shown by different style lines in both configurations. In this illustration, to represent the problem setting used to derive results in Section 4.2, we set  $\partial\mathcal{R}_p = \partial\mathcal{R}_s$  and  $\partial\mathcal{R}_i = \partial\mathcal{R}_u = \partial\mathcal{R}_a$ . However, this need not be the case. For example, the growth can occur only on a sub-region of  $\partial\mathcal{R}_u$ , as will be considered in Section 4.1, or the substrate can be permeable.

The deformation gradient is defined<sup>3</sup> as  $\mathbf{F} = \text{Grad}(\mathbf{x})$  with the Jacobian  $J = \det(\mathbf{F})$  representing the addition of volume due to solvent in the current configuration, and the displacement is given by  $\mathbf{u}(\mathbf{X}, t) = \mathbf{x}(\mathbf{X}, t) - \mathbf{X}$ . We thus refer to  $J$  as the swelling ratio and relate it to  $\phi^R$ , the solvent volume fraction in the reference configuration, by the incompressibility constraint

$$\phi^R = J - 1, \quad (1)$$

which assures that  $J = 1$  corresponds to the dry state. The solvent volume fraction in the current state can be recovered from the transformation  $\phi^R = J\phi$ .

The boundary of the body  $\mathcal{B}$  is denoted by  $\partial\mathcal{R}(t)$  in the current and  $\partial\mathcal{R}^R(t)$  in the reference configuration. We classify the different (and potentially overlapping) regions on this boundary as follows:  $\partial\mathcal{R}_u(t)$  - is the association boundary where the material is fixed to the substrate (i.e.  $\mathbf{u}$  is constrained),  $\partial\mathcal{R}_s(t)$  - is the unconstrained part of the boundary, which may be subjected to external traction,  $\partial\mathcal{R}_d(t)$  - is the boundary on which material can dissociate,  $\partial\mathcal{R}_a(t)$  - is the boundary on which material can associate,  $\partial\mathcal{R}_i(t)$  - is the impermeable region of the boundary, and  $\partial\mathcal{R}_p(t)$  - is the permeable region. Clearly,  $\partial\mathcal{R}_u(t) \cap \partial\mathcal{R}_s(t) = \emptyset$  and  $\partial\mathcal{R}_p(t) \cap \partial\mathcal{R}_i(t) = \emptyset$ , while  $\partial\mathcal{R}_d(t) \subset \partial\mathcal{R}_s(t)$  and  $\partial\mathcal{R}_a(t) \subset \partial\mathcal{R}_u(t)$ . The complete boundary can be represented either by  $\partial\mathcal{R}(t) = \partial\mathcal{R}_i(t) \cup \partial\mathcal{R}_p(t)$  or  $\partial\mathcal{R}(t) = \partial\mathcal{R}_u(t) \cup \partial\mathcal{R}_s(t)$ , as illustrated in Fig. 1. The boundary of the body can move in both the current and reference frames. If we denote a point on the boundary in the reference configuration by  $\mathbf{X}_b(t)$ , then its image in the current configuration is  $\mathbf{x}_b(t) = \mathbf{x}(\mathbf{X}_b(t), t)$ , and the corresponding velocities of the boundary in the reference and current configurations are

$$\mathbf{V}^R = \frac{d\mathbf{X}_b}{dt} \quad \text{and} \quad \mathbf{V} = \frac{d\mathbf{x}_b}{dt}, \quad (2)$$

respectively. These velocities can be related by  $\mathbf{V} = \mathbf{F}\mathbf{V}^R + \mathbf{v}$  where  $\mathbf{v} = \partial\mathbf{x}/\partial t$  is the material velocity. In particular, we denote the velocities of the association and dissociation boundaries by  $\mathbf{V}_a^R$  and  $\mathbf{V}_d^R$ , respectively.

<sup>3</sup>The operator  $\text{Grad}(\cdot)$  is the gradient with respect to the reference configuration, and  $\text{grad}(\cdot)$  the gradient with respect to the current configuration. Similarly, the operator  $\text{Div}(\cdot)$  is the divergence with respect to the reference configuration, and  $\text{div}(\cdot)$  the divergence with respect to the current configuration.

## 2.1. Balance laws and boundary conditions

In absence of body forces, momentum balance and corresponding boundary conditions read

$$\text{Div}(\mathbf{S}) = \mathbf{0} \quad \text{in} \quad \mathcal{R}^{\text{R}}(t), \quad (3)$$

$$\mathbf{u} = \bar{\mathbf{u}} \quad \text{on} \quad \partial\mathcal{R}_{\mathbf{u}}^{\text{R}}(t), \quad (4)$$

$$\mathbf{S} \cdot \mathbf{n}^{\text{R}} = \bar{\mathbf{s}} \quad \text{on} \quad \partial\mathcal{R}_{\mathbf{s}}^{\text{R}}(t), \quad (5)$$

where  $\mathbf{S} = \mathbf{S}(\mathbf{X}, t)$  is the first Piola–Kirchhoff stress tensor. In (4) we prescribe the displacement constraint on the association surface, such that  $\bar{\mathbf{u}}$  is determined by the growth process and the properties of the growth surface (as will be detailed in Section 3), and in (5) we write the stress free boundary condition on the free surface of the grown body, where  $\mathbf{n}^{\text{R}}$  represents the outward facing normal to the boundary in the reference configuration (see Fig. 1).

In absence of an external source, mass balance is written as (Abi-Akl et al., 2019a)

$$\dot{\phi}^{\text{R}} + \text{Div}(\mathbf{j}^{\text{R}}) = \mathbf{0} \quad \text{in} \quad \mathcal{R}^{\text{R}}(t), \quad (6)$$

$$\mu = \bar{\mu} \quad \text{on} \quad \partial\mathcal{R}_{\mu}^{\text{R}}(t), \quad (7)$$

$$-\mathbf{j}^{\text{R}} \cdot \mathbf{n}^{\text{R}} = \bar{j}^{\text{R}} \quad \text{on} \quad \partial\mathcal{R}_{\mathbf{j}}^{\text{R}}(t), \quad (8)$$

where  $\mathbf{j}^{\text{R}} = \mathbf{j}^{\text{R}}(\mathbf{X}, t)$  is the volumetric flux of solvent,  $\mu$  is the chemical potential that drives the flux (as described in the next section), and  $\bar{j}^{\text{R}}$  represents the penetrating flux through the inner side of the boundary. Although  $\partial\mathcal{R}_{\mathbf{j}}^{\text{R}}$  is impermeable, the transformation of solvent species into solid species at this boundary creates a solvent flux that is determined by requiring conservation of volume across the boundary

$$\bar{j}^{\text{R}} = (J - 1)\mathbf{V}^{\text{R}} \cdot \mathbf{n}^{\text{R}}. \quad (9)$$

Here it is assumed that the solvent outside of the body is stationary.

## 2.2. Constitutive relations

Following earlier studies (Chester and Anand, 2010; Abi-Akl et al., 2019a; Hong et al., 2008; Duda et al., 2010) that employ the Flory Rehner approach, the constitutive response of the two species material system can be described by its Helmholtz free energy per unit reference volume (Flory, 1942; Flory and Rehner, 1943)

$$\psi = \psi(\mathbf{F}, \phi^{\text{R}}), \quad (10)$$

which depends on the deformation of the solid network and concentration of solvent. Constitutive relations for the Piola Kirchhoff stress and the chemical potential are readily derived using the Coleman–Noll procedure on the dissipation rate to write

$$\mathbf{S} = \frac{\partial\psi}{\partial\mathbf{F}} - p\mathbf{J}\mathbf{F}^{-\text{T}} \quad \text{and} \quad \mu = \frac{\partial\psi}{\partial\phi^{\text{R}}} + p, \quad (11)$$

respectively. Here, the hydrostatic pressure  $p$  arises in response to the incompressibility constraint (1).

The solvent flux can be related to the gradient of chemical potential via a thermodynamically consistent kinetic law that satisfies the non-negativity of the dissipation rate, i.e.  $\mathbf{j}^{\text{R}} \cdot \text{Grad}\mu \leq 0$ . The specific response functions used in this work are detailed in Section 2.4.

Various forms of the coupled and nonlinear systems of governing equations described above have been solved numerically by several authors, to model the swelling of fluid permeated soft solids (Wang

et al., 2020; Liu et al., 2015b; Papastavrou et al., 2013b; Liu et al., 2015a; Hong et al., 2008; Chester et al., 2015; Truster and Masud, 2017), and different approaches have been proposed to simultaneously capture the effects of large deformations, incompressibility and swelling in bodies that are defined by a prescribed set of material points (i.e. with a constant  $\mathcal{R}^R$ ). An additional challenge in this work is imposed by the time evolution of the domain in both in the current and reference frames. This evolution is determined by a growth law, which too is nonlinearly coupled to the deformation and diffusion response, as detailed next.

### 2.3. Growth law

By specializing the dissipation rate to find the contribution on the boundary of the body, and restricting growth to occur along the normal to the surface in the reference frame a thermodynamically consistent law for the growth rate should obey the inequality (Abi-Akl et al., 2019a)

$$\int_{\partial\mathcal{R}^R} (\mathbf{S}\mathbf{n}^R \cdot \mathbf{F}\mathbf{n}^R + \Delta\psi + J\mu) V^R dA \geq 0, \quad (12)$$

where  $\mathbf{V}^R = V^R \mathbf{n}^R$ , and with the *latent energy of growth* defined as

$$\Delta\psi = \psi^+ - \psi^-, \quad (13)$$

where the superscripts  $(\cdot)^+$  and  $(\cdot)^-$  on a quantity denote its limiting values on the outer and inner side of the boundary, respectively. Since  $V^R$  is the rate of addition of solid mass (per unit area) we refer to it as the growth rate. From the above relation, it becomes apparent that the thermodynamic conjugate to this growth rate is

$$f = \mathbf{S}\mathbf{n}^R \cdot \mathbf{F}\mathbf{n}^R + \Delta\psi + J\mu, \quad (14)$$

which we refer to as the *driving force of growth*. We require that inequality (12) is obeyed in any sub-region of the boundary surface, namely the growth can be described by a kinetic relation  $V^R = \mathcal{G}(f)$  for which  $f\mathcal{G}(f) \geq 0$ .

### 2.4. Formulation summary and specific constitutive response

The formulation, written for an arbitrary set of constitutive response functions (i.e. the Helmholtz free energy  $\psi(\mathbf{F}, \phi^R)$ , the diffusion law, and the growth law  $\mathcal{G}(f)$ ) provides a complete representation of the time dependent evolution of the two species growing body, by obeying requirements of momentum balance (3) and mass conservation (6), and for a given set of boundary conditions (4), (5) and (7), (8). The specific forms of the constitutive response functions used to derive the numerical results in this work are detailed next. To compare the results of the present work with analytical results from the earlier study by Abi-Akl et al. (2019a), we apply the same constitutive response functions that were used therein.

For the response in the bulk, we employ the constitutive response functions which have been proposed for modeling large deformations in fluid permeated polymer networks (Chester and Anand, 2010; Duda et al., 2010; Hong et al., 2008). Accordingly, we decompose the free energy (10) into an elastic energy  $\psi_e$  due to deformation of the solid network and a mixing energy  $\psi_s$ , such that

$$\psi(\mathbf{F}, \phi^R) = \psi_e(\mathbf{F}) + \psi_s(\phi^R). \quad (15)$$

The elastic energy is taken as (Flory and Rehner, 1943; Flory, 1942)

$$\psi_e(\mathbf{F}) = \frac{G}{2} \left[ |\mathbf{F}|^2 - 3 - 2 \ln(\det \mathbf{F}) \right], \quad G = nkT, \quad (16)$$

where  $G$  is the shear modulus,  $n$  is the number of polymer chains per unit volume,  $k$  is the Boltzmann's constant, and  $T$  is the temperature. The energy of mixing is taken as

$$\psi_s(\phi^R) = \phi^R \left\{ \psi_0 + \frac{kT}{\nu} \left[ \ln \left( 1 - \frac{1}{1 + \phi^R} \right) + \frac{\chi}{1 + \phi^R} \right] \right\}, \quad (17)$$

where  $\chi$  is the Flory Huggins interaction parameter,  $\nu$  is the volume of a solution unit, and  $\psi_0$  is the reference free energy of the solution. On the dissociation boundary (i.e.  $\partial\mathcal{R}_d$ ) we can thus write  $\psi^+ = J\psi_0$  where multiplication by the volume ratio ( $J$ ) assures that the free energy is written per the same unit volume on either side of the boundary. On the association boundary (i.e.  $\partial\mathcal{R}_a$ ), a chemical binding potential  $\psi_a$  can locally alter the potential energy and represents the energetic gain due to association, hence (as in Abi-Akl et al. (2019a)) we take  $\psi^+ = \psi_a$ .

Substituting (15) with (16) and (17) into the constitutive relations (11), yields the constitutive response functions

$$\mathbf{S} = G(\mathbf{F} - \mathbf{F}^{-T}) - Jp\mathbf{F}^{-T}, \quad (18)$$

and

$$\mu = \mu_0 + \frac{kT}{\nu} \left[ \ln \left( 1 - \frac{1}{J} \right) + \frac{1}{J} + \frac{\chi}{J^2} \right] + p, \quad (19)$$

where  $\mu_0$  is the chemical potential of the surrounding fluid region. It is assumed to be constant, and in view of the incompressibility constraint is equal to the reference free energy (i.e.  $\mu_0 = \psi_0$ ). The above equation, allows us to write the pressure  $p$  in terms of the chemical potential in the useful form

$$p = \mu - \mu_0 - \frac{kT}{\nu} \left[ \ln \left( 1 - \frac{1}{J} \right) + \frac{1}{J} + \frac{\chi}{J^2} \right]. \quad (20)$$

A kinetic law for the solvent flux is chosen to obey the classical form Feynman et al. (1963), which in the reference frame reads

$$\mathbf{j}^R = -\frac{D\nu}{kT}(J-1)\mathbf{F}^{-1}\mathbf{F}^{-T}\text{Grad}\mu, \quad (21)$$

where  $D$  is the diffusion coefficient. This diffusion law further implies continuity of chemical potential across the permeable boundary. Hence,  $\bar{\mu} = \mu_0 = \mu^+ = \mu^-$  on  $\partial\mathcal{R}_p$ .

The kinetic law for growth is chosen to relate the rate of polymerization  $V^R$  to the driving force  $f$  of equation (14) using the classical Arrhenius form. Both association and dissociation reactions are considered in view of the dissipation inequality (12), by including two separate exponential terms, to write

$$V^R = \mathcal{G}(f) = \frac{b}{2} \left( e^{\frac{vf}{kT}} - e^{-\frac{vf}{kT}} \right) = b \sinh \left( \frac{vf}{kT} \right), \quad (22)$$

where  $b > 0$  is the reaction constant.

In summary, the constitutive response depends on a set of seven material parameters:  $G$ ,  $\nu$ ,  $\chi$ ,  $\psi_0$ ,  $\psi_a$ ,  $D$ ,  $b$  and assuming room temperature we have  $kT = 4 \times 10^{-21}$  J. For the derivation of results in this work, we use values in the common range (Chester and Anand, 2010; Hong et al., 2008; Lai and Hu, 2018) for parameters that describe the bulk response  $G = 4$  kPa,  $\nu = 10^{-28}$  m<sup>3</sup>,  $\chi = 0.2$ ,  $\psi_0 = -0.4$  MPa,  $D = 10^{-4}$  m<sup>2</sup> s<sup>-1</sup>. Parameters that describe the growth kinetics are taken as  $\psi_a = -13$  MPa, and  $b = 10^{-7}$  m s<sup>-1</sup>. The sensitivity analysis in this work will center on varying the boundary conditions to examine the effect of geometry on the growth process.

### 3. Numerical implementation

In addition to the geometric nonlinearities arising from the very large deformations, the governing equations (3)-(5) and (6)-(8) unveil several nonlinearities in the coupling mechanisms between the deformation and the chemical potential. On the one hand, an increase (decrease) of the chemical potential contributes to pressure build-up (drop) in the bulk material. On the other hand, the deformation of the bulk affects the diffusivity through the bulk via the chemical potential. Moreover, both the deformation and the chemical potential contribute to the driving force of growth (14), which dictates the velocity of the boundary and constitutes an additional source of nonlinearity. In this section we propose a numerical scheme that addresses the challenges emerging in the simulation of this complex response.

#### 3.1. Weak form of the governing equations

Equations (3)-(5) and (6)-(8) represent two, coupled, boundary value problems for the primal unknowns  $\mathbf{u}$  and  $\mu$ . We introduce the test functions  $\mathbf{w}$  and  $q$  for the displacement and for the chemical potential, respectively, which vanish on  $\partial\mathcal{R}_{\mathbf{u}}$  and  $\partial\mathcal{R}_{\mu}$ , respectively, and obtain the following weak formulations of the boundary value problems

$$\int_{\mathcal{R}^R(t)} \mathbf{S}(\mathbf{u}, \mu) : \text{Grad } \mathbf{w} \, dv = \int_{\partial\mathcal{R}_s^R(t)} \bar{\mathbf{s}} \cdot \mathbf{w} \, da \quad \forall \mathbf{w}, \quad (23)$$

and

$$\int_{\mathcal{R}^R(t)} \mathbf{j}^R(\mathbf{u}, \mu) \cdot \text{Grad } q \, dv - \int_{\mathcal{R}^R(t)} Jq \, dv - \int_{\partial\mathcal{R}_f^R(t)} (J-1) V^R q \, da = 0 \quad \forall q, \quad (24)$$

where we have used (9), to express the conservation of volume at the boundary, and (1), to express the material incompressibility. In the above integral representation, we have highlighted the dependence of the stress tensor  $\mathbf{S}$  and the flux  $\mathbf{j}^R$  on the primal variables  $\mathbf{u}$  and  $\mu$ . We recall that  $\mathbf{S}(\mathbf{u}, \mu)$  and  $\mathbf{j}^R(\mathbf{u}, \mu)$  are given by (18)-(20), which we rewrite in the form

$$\mathbf{S}(\mathbf{u}, \mu) = G \left( \mathbf{F} - \mathbf{F}^{-T} \right) - J \left( \mu - \mu_0 - \frac{kT}{v} \left[ \ln \left( 1 - \frac{1}{J} \right) + \frac{1}{J} + \frac{\chi}{J^2} \right] \right) \mathbf{F}^{-T},$$

and

$$\mathbf{j}^R(\mathbf{u}, \mu) = -\frac{Dv}{kT} (J-1) \mathbf{F}^{-1} \mathbf{F}^{-T} \text{Grad} \mu,$$

where  $\mathbf{F} = \text{Grad}(\mathbf{u}) - \mathbf{I}$  and  $J = \det(\text{Grad}(\mathbf{u}) - \mathbf{I})$ .

#### 3.2. Time discretization

We propose an iterative algorithm to advance the solution from time  $t$  to time  $t + \Delta t$ . We employ a first-order discretization of the time derivatives to approximate  $\dot{J}$  at time  $t + \Delta t$  as

$$\dot{J}(t + \Delta t) \approx \frac{J(t + \Delta t) - J(t)}{\Delta t},$$

and the boundary velocity  $\mathbf{V}^R$  in (2) at time  $t + \Delta t$  as

$$\mathbf{V}^R(t + \Delta t) = \frac{d\mathbf{X}_b}{dt}(t + \Delta t) \approx \frac{\mathbf{X}_b(t + \Delta t) - \mathbf{X}_b(t)}{\Delta t}.$$



Since the time scale of diffusion is significantly faster than that of growth, we treat equations (23) and (24) in a fully-coupled fashion, while decoupling them from the time evolution of the domain  $\mathcal{R}^R(t)$ . We have verified that this approach and the results shown in Section 4 are at convergence with respect to the time step, which confirms that for sufficiently small time steps the evolution of the domain  $\mathcal{R}^R(t)$  can be treated explicitly without loss of accuracy.

At time  $t + \Delta t$ , we seek the displacement field  $\mathbf{u}(t + \Delta t)$  and the chemical potential field  $\mu(t + \Delta t)$  which satisfy the following set of equations

$$\int_{\mathcal{R}^R(t)} \mathbf{S}(\mathbf{u}(t + \Delta t), \mu(t + \Delta t)) : \text{Grad } \mathbf{w} \, dv = \int_{\partial \mathcal{R}_s^R(t)} \bar{\mathbf{s}} \cdot \mathbf{w} \, da \quad \forall \mathbf{w}, \quad (25)$$

$$\begin{aligned} \int_{\mathcal{R}^R(t)} \mathbf{j}^R(\mathbf{u}(t + \Delta t), \mu(t + \Delta t)) \cdot \text{Grad } q \, dv - \int_{\mathcal{R}^R(t)} \frac{J(t + \Delta t) - J(t)}{\Delta t} q \, dv \\ - \int_{\partial \mathcal{R}_f^R(t)} (J(t + \Delta t) - 1) V^R(t + \Delta t) q \, da = 0 \quad \forall q. \end{aligned} \quad (26)$$

To solve the problem in a fully-coupled fashion we adopt a Newton-Raphson iterative algorithm to advance from one nonlinear iteration to the next until convergence, starting from initial guesses for  $\mathbf{u}$  and  $\mu$  given by the converged solutions at time  $t$ .

Upon convergence, we update the domain  $\mathcal{R}^R(t)$  by updating its boundary with

$$\mathbf{X}_b(t + \Delta t) = \mathbf{X}_b(t) + \Delta t V^R(t + \Delta t) \mathbf{n}^R(t), \quad (27)$$

where the velocity  $V^R(t + \Delta t)$  is computed in terms of the newly updated displacement  $\mathbf{u}(t + \Delta t)$  and chemical potential  $\mu(t + \Delta t)$ . The new domain is then remeshed, as described in the next section. The algorithm to update the displacement, chemical potential and problem domain from time  $t$  to time  $t + \Delta t$  is further summarized in Algorithm 1.

### 3.3. Space discretization and growth

Our numerical simulations consider the growth of a body with an initially rectangular cross-section of dimensions  $w^R \times l^R$  (in the reference configuration), and assumes generalized plane-strain conditions, such that the motion occurs only in the plane of the cross-section, i.e. in the  $(X_1, X_3)$  plane. The association surface spans the width  $w^R$  along the  $X_1$  direction and the initial length, along  $X_3$ , is  $l^R$ . We take advantage of the symmetry of the problem to resolve only half of the domain<sup>4</sup>.

We perform the space discretization by introducing a triangular mesh of the computational domain  $\mathcal{R}^R$ . The dimensions of the domain in which growth occurs, i.e.  $w^R$  and  $l^R$ , are each divided into 10 elements across with further refinement near the edges. The dimension along  $X_2$  is divided into 2 elements and appropriate boundary conditions with no displacements or flux applied to maintain generalized plane-strain conditions. First order shape functions are used for the chemical potential  $\mu$  and second order shape functions for the displacement  $\mathbf{u}$ .

As discussed in Section 3.2, we solve the fully-coupled set of equations for the displacement and chemical potential with a Newton-Raphson nonlinear solver. We solve the linearized system with a

---

<sup>4</sup>We have confirmed that solution over the entire domain leads to identical results.

direct solver for the sake of robustness. More precisely, because the fully-coupled linear system is not symmetric we use a LU-factorization solver for the linear steps. Upon convergence of the non-linear solver we evaluate the growth velocity at the boundary and accommodate growth by redefining the domain and creating a new mesh at every time step, based on the solution at the previous time. Note that this requires to reinterpolate the newly computed swelling ratio  $J(t + \Delta t)$  on the new computational domain  $\mathcal{R}^R(t + \Delta t)$  so that the second integral in Equation (26) can be computed. Since the finite element mesh is three dimensional while in the considered generalized plane-strain deformation pattern motion is only permitted in the plane, the growth is reduced to two dimensions. Namely, only a grown/dissociated surface of incremental thickness is defined at every time step and then extruded in its normal direction following a volume conserving regularization procedure, as detailed next and illustrated on Fig. 2.

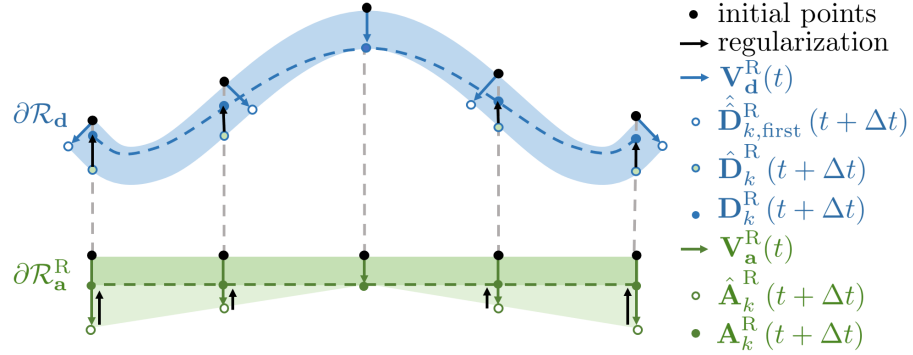


Figure 2: Schematic showing the construction of the boundaries of the body in the next time step and the volume preserving regularization.

At every time step, the association boundary in the reference configuration is defined by  $N$  points,  $\mathbf{A}_1^R(t), \dots, \mathbf{A}_N^R(t)$ , and the dissociation boundary in the reference configuration by  $N$  points,  $\mathbf{D}_1^R(t), \dots, \mathbf{D}_N^R(t)$ . Since motion is not permitted along  $X_2$ , the values of  $A_{k,2}^R$  and  $D_{k,2}^R$  are constant in time.

The association boundary of the new domain is determined via two steps. The intermediate step is

$$\hat{\mathbf{A}}_k^R(t + \Delta t) = \mathbf{A}_k^R(t) + V_{\mathbf{a},k}^R(t) \cdot \Delta t \cdot \mathbf{n}_{\mathbf{a},k}^R, \quad \forall k = 1, \dots, N, \quad (28)$$

where the superimposed ( $\hat{\cdot}$ ) denotes the fact that this is an intermediate value, and with the index  $k$  going through all  $N$  nodes that lie on  $\partial\mathcal{R}_a^R$ . Given the fixed boundary condition on the association surface, the normal vectors are constant and given by

$$\mathbf{n}_{\mathbf{u},k}^R = (0, 0, -1)^T, \quad \forall k = 1, \dots, N. \quad (29)$$

The dissociation boundary of the new domain is determined via three steps. The first intermediate step is

$$\hat{\mathbf{D}}_k^R(t + \Delta t) = \mathbf{D}_k^R(t) + V_{\mathbf{d},k}^R(t) \cdot \Delta t \cdot \mathbf{n}_{\mathbf{d},k}^R(t), \quad \forall k = 1, \dots, N, \quad (30)$$

with the index  $k$  going through all  $N$  nodes that lie on  $\partial\mathcal{R}_d^R$ . Unlike the association surface, the morphology of the dissociation surface changes in time and the normal vectors  $\mathbf{n}_{\mathbf{d},k}^R$  are calculated newly at every time step. The unnormalized vectors are defined as the outward pointing vector perpendicular to

the connecting edge between the next and the previous node

$$\hat{\mathbf{n}}_{\mathbf{d},k}^{\mathbf{R}}(t) = \begin{cases} \mathbf{R} \cdot (\mathbf{D}_{k+1}^{\mathbf{R}}(t) - \mathbf{D}_k^{\mathbf{R}}(t)), & \text{if } k = 1, \\ \mathbf{R} \cdot (\mathbf{D}_{k+1}^{\mathbf{R}}(t) - \mathbf{D}_{k-1}^{\mathbf{R}}(t)), & \text{if } k = 2, \dots, N-1, \\ \mathbf{R} \cdot (\mathbf{D}_k^{\mathbf{R}}(t) - \mathbf{D}_{k-1}^{\mathbf{R}}(t)), & \text{if } k = N, \end{cases} \quad (31)$$

with the rotation matrix

$$\mathbf{R} = \begin{bmatrix} 0 & 0 & 1 \\ 0 & 1 & 0 \\ -1 & 0 & 0 \end{bmatrix}, \quad (32)$$

and are then normalized to yield

$$\mathbf{n}_{\mathbf{d},k}^{\mathbf{R}}(t) = \frac{\hat{\mathbf{n}}_{\mathbf{d},k}^{\mathbf{R}}(t)}{|\hat{\mathbf{n}}_{\mathbf{d},k}^{\mathbf{R}}(t)|}. \quad (33)$$

Depending on the direction of the normal vectors, it is now possible that some points obtained from the first intermediate step (30) have  $\hat{D}_{k,1}^{\mathbf{R}}(t + \Delta t)$  outside the body in the reference configuration (Fig. 2). To avoid this, without loss of generality, we define the points to align with the initially defined locations in the  $X_1$  direction, such that  $D_{k,1}^{\mathbf{R}}(t) = D_{k,1}^{\mathbf{R}}(0)$ . To this end, the function  $\hat{D}_{k,3}^{\mathbf{R}}(t + \Delta t) = f(\hat{D}_{k,3}^{\mathbf{R}}(t + \Delta t))$  is linearly inter- and extrapolated to obtain  $\hat{\mathbf{D}}_k^{\mathbf{R}}(t + \Delta t)$ .

Since the association boundary is subjected to a fixed boundary condition, its shape in the current configuration is preserved over time. Its shape in the reference configuration, however, is only preserved over time if the growth rate (i.e.  $V_{\mathbf{a},k}^{\mathbf{R}}(t) \cdot \Delta t \cdot \mathbf{n}_{\mathbf{a},k}^{\mathbf{R}}(t)$ ) is uniform for all points  $k$  on the association boundary. If growth is not uniform, morphing of the association boundary in the reference configuration leads to residual stresses. Yet, to reduce the complexity in the present numerical model, we constrain the system to produce only uniform growth. We implement this assumption by including a volume preserving regularization in determining the reference location of the boundaries in the next time step

$$D_{k,3}^{\mathbf{R}}(t + \Delta t) = \hat{D}_{k,3}^{\mathbf{R}}(t + \Delta t) + \hat{A}_{k,3}^{\mathbf{R}}(t + \Delta t) - \hat{A}_{0,3}^{\mathbf{R}}(t + \Delta t), \quad \forall k = 1, \dots, N, \quad (34)$$

$$A_{k,3}^{\mathbf{R}}(t + \Delta t) = \hat{A}_{0,3}^{\mathbf{R}}(t + \Delta t), \quad \forall k = 1, \dots, N, \quad (35)$$

where  $\mathbf{A}_0^{\mathbf{R}}$  is the point where the growth is minimal.

Although this regularization omits the physical effects that may arise in response to nonuniform growth. This assumption is exact for a chemically uniform association surface, at both the limits of an infinitely long substrate  $w/l \rightarrow \infty$  (i.e. uniaxial growth) and a very thin substrate  $w/l \rightarrow 0$  (i.e. filament growth). For the present simulations, it will be shown, by post evaluation (in Section 4.3), that this effect is negligible in all of the considered settings. Nonetheless, future work will expand on the present framework to account for these effects, which may become significant if the chemical properties of the growth surface are nonuniform.

### 3.4. Initialization of the solution procedure

The iterative procedure described in Section 3.2 and summarized in Algorithm 1 has to be initialized with an initial condition. Finding the initial equilibrium configuration is a non trivial task, which requires a preliminary iterative scheme that we discuss in this section.

---

**Algorithm 1** Update of displacement  $\mathbf{u}$ , chemical potential  $\mu$ , and computational domain  $\mathcal{R}$  at every time step.

---

Given  $J(t)$  and  $\mathcal{R}^R(t)$ , do:

1. Compute the updated  $\mathbf{u}(t + \Delta t)$  and  $\mu(t + \Delta t)$  by solving the fully-coupled nonlinear problem (25) and (26) on  $\mathcal{R}^R(t)$ ;
  2. Update  $\mathbf{F}(t + \Delta t)$ ,  $\mathbf{S}(t + \Delta t)$ ,  $J(t + \Delta t)$  based on  $\mathbf{u}(t + \Delta t)$ ;
  3. Compute the updated boundary velocity  $V^R(t + \Delta t)$  from Equation (22) based on  $\mathbf{u}(t + \Delta t)$  and  $\mu(t + \Delta t)$ ;
  4. Update the position of the boundary nodes as detailed in Section 3.3 to obtain  $\mathcal{R}^R(t + \Delta t)$ ;
  5. Remesh the new domain  $\mathcal{R}^R(t + \Delta t)$  to obtain the new computational domain;
  6. Reinterpolate the newly computed swelling ratio  $J(t + \Delta t)$  on the updated computational domain  $\mathcal{R}^R(t + \Delta t)$ ;
  7. Proceed to next time step.
- 

As a first step, the boundary and initial conditions must be prescribed. A characteristic of the growth surface is the density of solid material formed on it, which can be determined, for example, by the distribution of chemical binding sites. Hence, the in-plane stretch components  $(\bar{\lambda}_1, \bar{\lambda}_2) = (\bar{\lambda}_1, \bar{\lambda}_2)(X_1, X_2)$  must be given as a boundary condition. For the present simulation we consider a uniform and isotropic in-plane stretch  $\bar{\lambda}_1 = \bar{\lambda}_2 = \lambda_0$  and thus the in-plane components of the boundary constraint in (4) are given by  $\bar{u}_1 = (\lambda_0 - 1)X_1$  and  $\bar{u}_2 = (\lambda_0 - 1)X_2$ , while the out of plane displacement is determined to accommodate the growth, such that  $\bar{u}_3 = -X_3$ , and thus  $x_3 = 0$  on the growth surface. Here the symmetry surface is defined along  $X_3$  and  $x_3$ .

Due to initial swelling and the constraint to the substrate, the initial configuration itself is not a trivial homogeneous state, and thus a preliminary numerical scheme is applied to recover the initial state before allowing growth to commence. To achieve convergence of the strongly coupled and highly nonlinear system, the preliminary scheme is divided into three steps, as illustrated in Fig. 3. The *first step* initiates from the homogeneous dry state with  $\mathbf{F} = \mathbf{I}$  and with the simplified boundary conditions adapted to represent the uniaxial field by replacing the chemical potential boundary condition (7) with a displacement boundary condition on  $\partial\mathbf{R}_p \setminus \partial\mathbf{R}_d$  to allow motion only along  $x_3$ . We then proceed in a step-wise manner to accommodate swelling, where each integration step takes as initial guess the result from the previous step<sup>5</sup>. Further, this initial step solves only a linearized version of the constitutive equations (as described in the Appendix). In the *second step*, the same system is solved with the fully nonlinear equations while  $\lambda_1$  and  $\lambda_2$  are raised incrementally to the target value  $\lambda_0$ . Finally, in the *third*

---

<sup>5</sup>Note that in the preliminary scheme, depending on the number of integration steps, the diffusion need not be fully equilibrated.

step the appropriate boundary conditions are used to obtain the solution for the full 2D geometry.

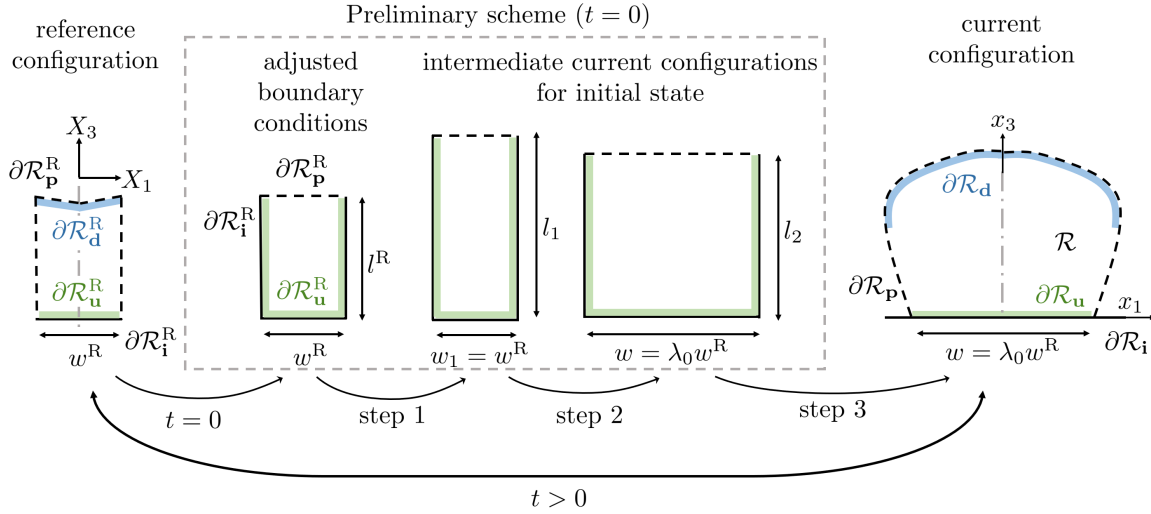


Figure 3: Illustration of the problem setting in current and reference frames, and preliminary scheme for derivation of initial current configuration via three steps. In the initial reference configuration the layer has a dry length of  $l^R$  and the dry width of the association surface is  $w^R$ . The current width is  $w = \lambda_0 w^R$ . Through the growth process the width of the association surface is held constant in both frames, while  $l^R = l^R(X_1, t)$ .

Once the preliminary scheme is complete, we proceed to perform the time integration for the growth process, as described in Section 3.2. Note that in contrast to kinematic growth theories, here no intermediate growth configuration is needed, as both the current and reference configurations evolve simultaneously<sup>6</sup>.

## 4. Results

In this section, we apply the presented numerical growth simulation framework to four different settings. First, we verify the numerical framework and compare our results with the analytical results obtained by Abi-Akl et al. (2019a) for uniaxial growth. Then, we proceed to describe growth in two dimensions, varying the substrate properties, as defined by the stretch  $\lambda_0$  and the width of the association surface  $w^R$ . All other parameter values are kept constant in the presented simulations.

The model is built on the two open-source software components: Fenics, a Finite Element Method (FEM) software library (Logg et al., 2012; Alnæs et al., 2015); and Gmsh, a 3D finite-element mesh generator (Geuzaine and Remacle, 2009). The output is then processed using the open-source large data visualization tool Paraview (Ahrens et al., 2005).

### 4.1. Uniaxial growth

The theoretical model detailed in Section 3 can be solved analytically in simplified geometric settings. Abi-Akl et al. (2019a) obtained an analytical solution for growth on a flat substrate where the association surface is unbounded in the  $X_1$  and  $X_2$  directions such that growth occurs only along  $X_3$ .

<sup>6</sup>An intermediate configuration is often used in kinematic growth theories via multiplicative decomposition of the deformation gradient (Menzel and Kuhl, 2012).

Later, this analytical solution was extended to account for the effect of curvature and substrate deformation, by considering radial growth on deformable spherical substrates (Abi-Akl and Cohen, 2020). In all cases, it was found that following a rapid diffusion dominated response, the growth process tends towards a *universal path* that is independent of initial conditions. Along this universal path growth and diffusion act harmoniously as the system evolves towards a *treadmilling* state. In this treadmilling state, association and dissociation are balanced such that the body no longer changes its dimensions in the current frame, although association and dissociation reactions persist. In this section, as a validation of our numerical model, we consider uniaxial growth on a flat substrate and compare our results with the analytical results from Abi-Akl et al. (2019a).

To constrain the growth to occur only along the  $X_3$  direction, we subject the faces of the rectangular body with  $\mathbf{n}^R = (0, 0, \pm 1)$ , to the displacement boundary condition (4) such that  $\bar{u}_1 = \bar{u}_2 = 0$ , and render them impermeable by applying the boundary condition (8) with  $\bar{\mathbf{j}}^R = 0$ , as illustrated in Fig. 4(a). We permit association only on the substrate where  $\mathbf{n}^R = (0, 0, -1)$ .

Simulations for layers with different initial lengths ( $l^R$ ) were conducted, spanning the time it takes for diffusion to equilibrate (the width  $w^R$  does not effect these results), and are represented by the points in Fig. 4(b). It is expected that the points coincide with the universal path, which is obtained via the analytical solution, and represented by the black curve. The remarkable agreement, observed for all cases, provides a validation of our numerical scheme. In the next section we will expand on these simulations by removing the vertical constraint and allowing for two-dimensional morphologies to emerge.

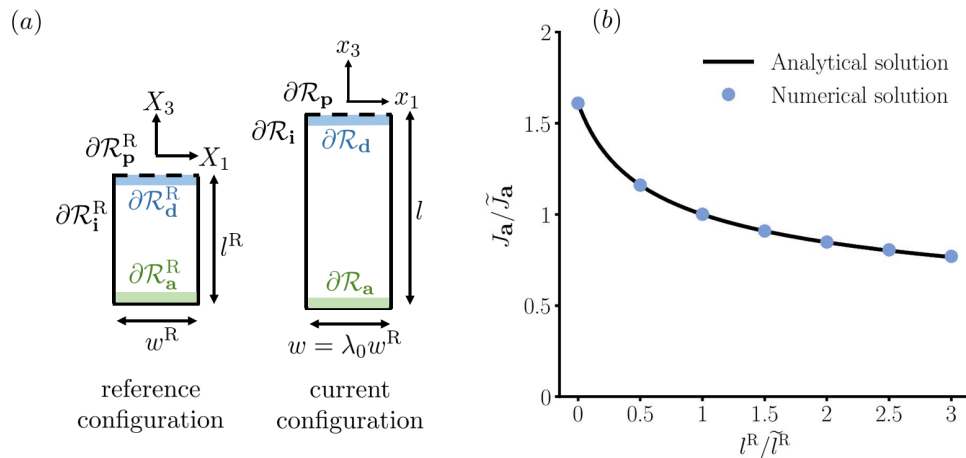


Figure 4: (a) Illustration of reference and current configurations for the case of uniaxial growth, as well as corresponding boundary conditions. Here  $\partial\mathcal{R}_p = \partial\mathcal{R}_s$  and  $\partial\mathcal{R}_i = \partial\mathcal{R}_u$ . (b) Comparison of analytical universal path from Abi-Akl et al. (2019a) with numerical simulation results, showing the swelling ratio at the association surface ( $J_a$ ) as a function of the dry length ( $l^R$ ). Both are normalized by their treadmilling values, as denoted by the superimposed tilde. These results are obtained using  $\lambda_0 = 4.96$ .

#### 4.2. Two-dimensional growth

In the following, we present results for the evolution of a 2D growing system and discuss the sensitivity of the growth process to the two parameters  $\lambda_0$  and  $w^R$ , which are properties of the growth surface. The current and reference configurations in the 2D setting are illustrated in Fig. 1 and later also in Fig. 3, where additional details on the geometry are provided. Here we consider growth scenarios for which we set  $\partial\mathcal{R}_p = \partial\mathcal{R}_s$  and  $\partial\mathcal{R}_i = \partial\mathcal{R}_u = \partial\mathcal{R}_a$ . In contrast to the uniaxial setting, described

in the previous section, flux is now permitted through the  $\mathbf{n}^R = (0, \pm 1, 0)$  faces, which are no longer geometrically constrained.

A representative simulation of the growth process in the current frame is shown in Fig. 5 for a sample with  $w^R = 2$  mm, and  $\lambda_0 = 4.88$ . At  $t = 0$  the swollen sample begins to associate/dissociate at its boundaries. Due to the transformation of solvent into solid material at the association surface, the solvent content and hence the swelling ratio  $J$  is smallest in that region. At the permeable boundary, continuity of chemical potential leads to a high solvent content and a larger swelling ratio  $J$ , with the maximum value occurring at the corners. The shape that is developed over time depends on the fully coupled response of the material system. As observed, the net association is maximum at the mid-section, leading to thickening there, while the net association appears to be minimal near the edges. This is due to the competition between association and dissociation, and is highly affected by both the local fields and the orientation of the surface normal, which act together to define the final morphology of the growing body. A representative mesh (recall that a new mesh is formed at every time step) is shown for  $t = 46$  h, as well as the corresponding reference configuration at that time. The large deformations that occur between the two configurations lead to significant nonlinear effects that are fully captured by the present framework.

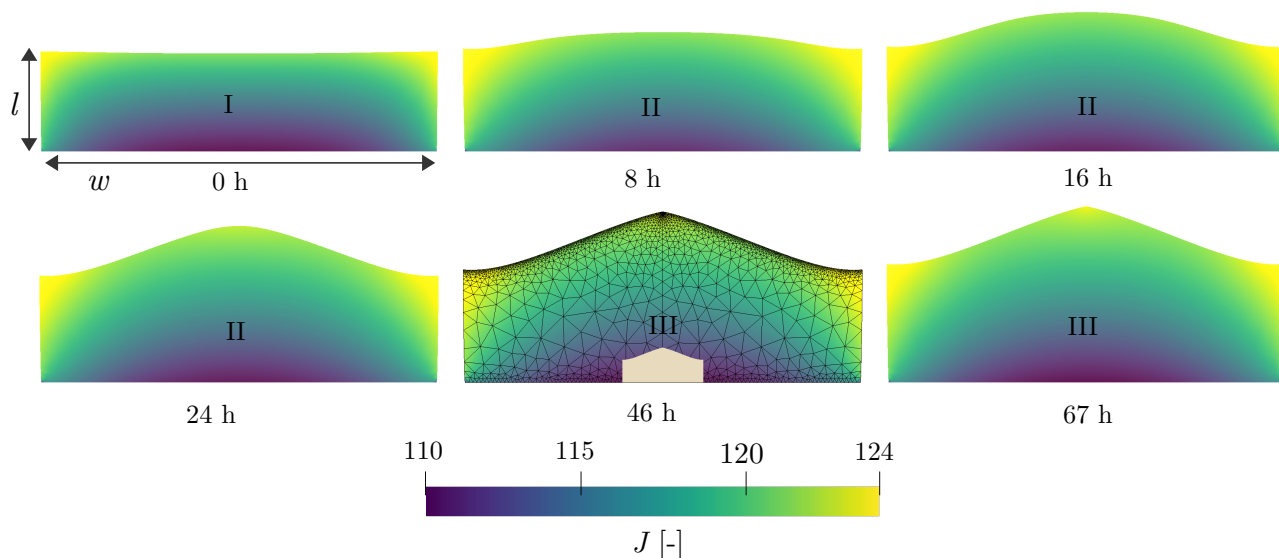


Figure 5: Results for  $w^R = 2$  mm and  $\lambda_0 = 4.88$  in the current configuration, with  $w = \lambda_0 w^R$  and the thickness  $l$ , at the edge evolving from 2.5 mm to 2.8 mm. At time  $t = 46$  h, the mesh and the reference configuration are included in the image. (I) denotes the diffusion-dominated stage, (II) the morphogenesis stage, and (III) the proportionate growth stage. Here the color map represents the swelling ratio  $J$ , corresponding images portraying changes in chemical potential are shown in Fig. A1 of the Appendix. A video of the simulation is provided in the [supplementary material](#).

In examining the growth process we identify four stages: (I) a *diffusion-dominated* stage, in which large and rapid adaptations in swelling,  $J$ , occur in response to the sudden change in boundary conditions, (II) a *morphogenesis* stage, in which changes in morphology are observed while relatively small changes in swelling occur, (III) a *proportionate growth* stage, in which the morphology of the dissociation surface and the swelling field,  $J$ , are nearly unchanged while the dimension of the body continues to evolve by homogeneous addition and removal of material at the association/dissociation surfaces, and (IV) a *treadmilling* state, in which both the morphology and the spatial fields remain constant in

time. The last stage is approached asymptotically, and will be discussed in more detail in the next paragraph. In contrast to uniaxial growth, which, as explained in the previous section, consists of three stages, the morphogenesis stage emerges here due to the additional degree of freedom in the deformation field, whereas the proportionate growth stage is a 2D analogue of the universal path, which has been observed in the uniaxial settings.

The different stages of growth (i.e. stages I-III) have been consistently observed in all of our simulations and are further clarified in Fig. 6, by comparing the morphological evolution of the body shown in Fig. 5 with that of a body grown on a substrate with the same width  $w^R = 2$  mm, but with a slightly different imposed stretch  $\lambda_0 = 4.907$ . In both cases, the morphology that emerges after the diffusion dominated stage is shown to be nearly rectangular (yellow regions). Morphogenesis then dominates and occurs for approximately  $t \sim 46$  h in both samples. It results in significant thickening of the layer in the mid region, with minimal net growth near the edges. Interestingly, following this morphogenesis, the layer with  $\lambda_0 = 4.907$  appears to directly approach the treading state, while the layer with  $\lambda_0 = 4.88$  continues to thicken for the duration of the simulation, but without any appreciable changes in its morphology. The time required for this proportionate growth stage to approach treading is determined by the chosen initial thickness  $l^R$ . For the sample with  $\lambda_0 = 4.907$ , this initial thickness matches the final treading thickness at the edges, thus significantly reducing the time needed to arrive at full treading, by factually skipping the proportionate growth stage. The same initial thickness for the sample with  $\lambda_0 = 4.88$  first transcends into the proportionate growth stage at 46 h and remains in that stage for the rest of the simulated timeframe, with approximately constant net growth velocity  $\dot{l}^R$ . It can be assumed that this sample will also reach treading eventually. However the evolution up to this point occurs on a timescale much larger than the one investigated in this work. The amount of time it takes to complete morphogenesis is the same for both samples, however the path of the two settings differs largely once the shape is formed. This result also exemplifies the significant sensitivity of the growth process to the imposed stretch,  $\lambda_0$ .

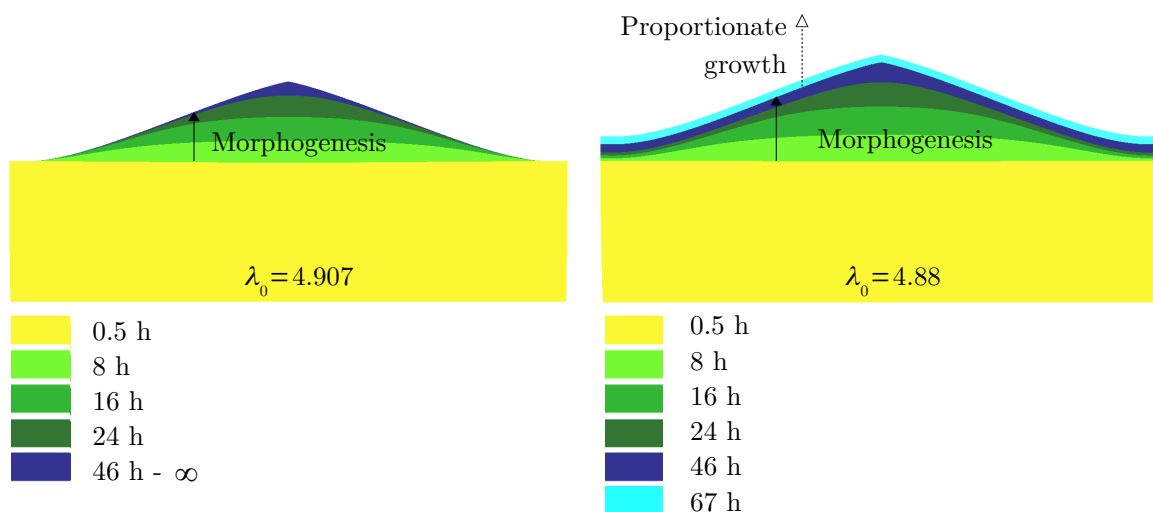


Figure 6: Comparison of results for  $\lambda_0 = 4.907$  against  $\lambda_0 = 4.88$ , obtained with  $w^R = 2$  mm and shown in the current configuration.



Quite remarkably, the four stages of growth observed in our simulations are reminiscent of growth processes in the natural world, and yet emerge here spontaneously without any externally imposed regulation or coordination. Skin repair, for example, consists of a sequence of well defined phases (Lucas et al., 2010; Sorg et al., 2017): the early stage is characterized by an immediate influx of growth factors; this is followed by the formation of tissue that fills the wound; then, when the wound space is refilled and the epidermis is restored, the final stage, consists of tissue maturation. These three phases are analogous to stages I-III in our simulations, while the final healthy result is the treadmilling state (IV).

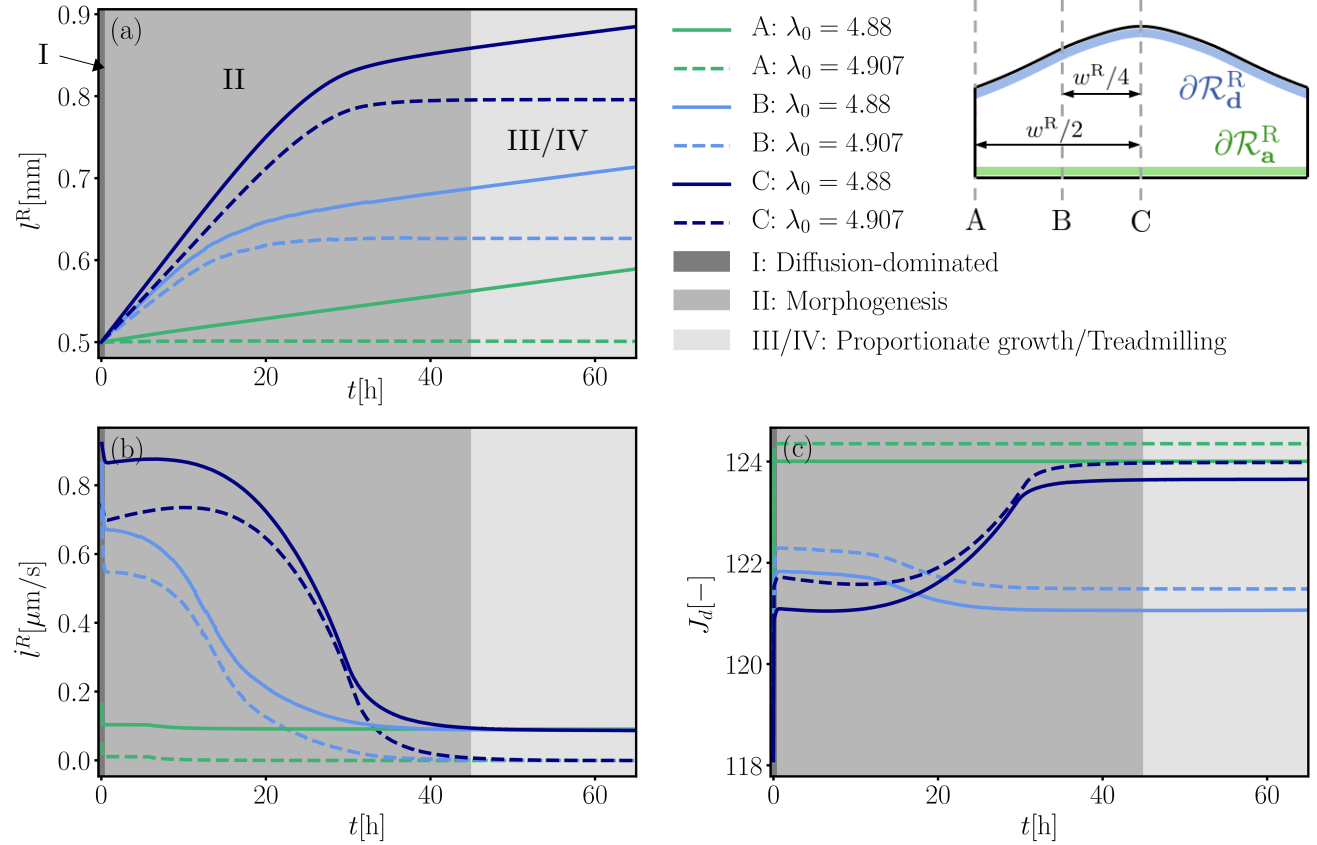


Figure 7: Sensitivity to prestretch  $\lambda_0$  is shown by examining the evolution of (a) the dry length  $l^R$ , (b) its rate of change  $j^R$ , and (c) the swelling ratio at the dissociation surface  $J_d$ , for the simulations shown in Figs. 5 and 6 at three different locations, denoted by A, B, C as illustrated in the inset.

To better understand the sensitivities of the growth process, the results in Figs. 5 and 6 are further examined in Fig. 7 showing the evolution of the normalized dry length  $l^R$ , its rate  $j^R$ , and the swelling ratio at the dissociation surface  $J_d$ , for two different values of the prestretch  $\lambda_0$ , and at three different locations; A - the edge, B - the mid line, and C - the symmetry surface (as illustrated). Both configurations undergo a fast diffusion-dominated stage I in the first 0.5 h before they transcend into the morphogenesis stage II. After 46 h, the simulation with  $\lambda_0 = 4.88$  arrives at the proportionate growth stage III, where for the duration of the simulation the value of  $j^R$  remains approximately constant. It can be assumed that, if significantly longer simulation times are considered, it will further develop towards treadmilling. The material with larger prestretch  $\lambda_0 = 4.907$  also completes morphogenesis at 46 h, but

after this directly approaches the treadmilling state (i.e. stage IV). Fig. 7(c) shows that after initial diffusion,  $J_d$  continues to evolve only during stage II. Since changes in the orientation of the dissociation surface directly influence the value of  $J_d$ , this further confirms that morphogenesis is dominant only in stage II. Later,  $J_d$  approaches a constant value. Notice that during morphogenesis,  $J_d$  remains constant at A, it increases at the symmetry surface and becomes smaller in-between (at B).

Next, we investigate the sensitivity of the model to the width of the association surface  $w^R$ . Figs. 8(a,b) show the evolution of dry length over time as well as the (approximate) treadmilling length for different values of  $w^R$ . Fig. 8(c) shows the (approximate) treadmilling morphologies of bodies grown on substrates with different width  $w^R$ . A larger width of the association surface results in a larger final length, which, as shown in Fig. 8(b), exhibits a linear relation. However, since the analysis is limited to four example cases, it is possible that this observed linearity is limited to the considered region dimensions. Finally, from these results it is evident that the width of the association surface is a well-suited tool to control the final dimensions of the grown material.

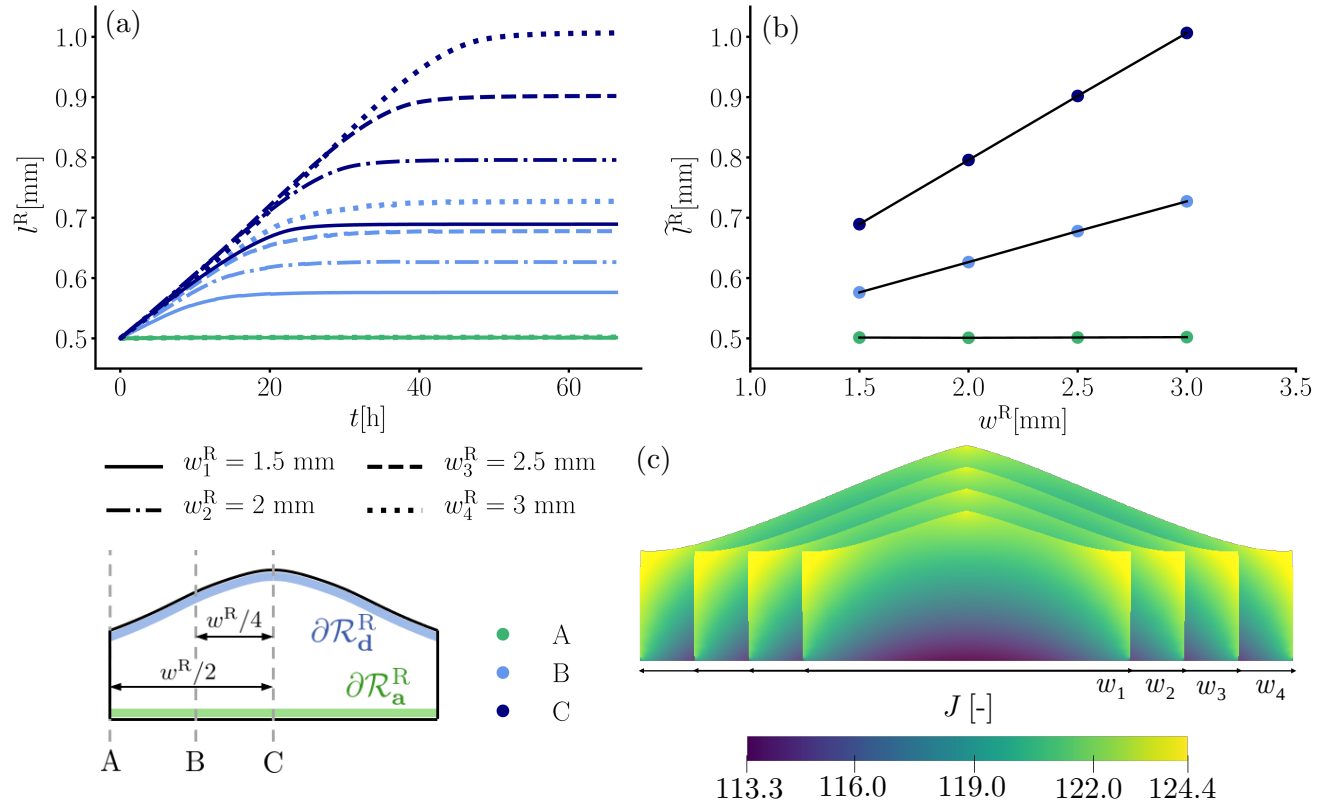


Figure 8: Material evolution for different dry widths  $w^R$  with prestretch  $\lambda_0 = 4.907$  and  $w = \lambda_0 w^R$ . (a) Evolution of dry length at the border (A), the mid-surface (B), and the symmetry surface (C). (b) Approximate treadmilling length as a function of  $w^R$ . (c) Approximate treadmilling states, represented in the current configuration.

To further understand the dynamics that lead to the morphological and proportionate changes observed in our simulations, it is insightful to examine the association and dissociation velocities and how they vary both with time, and along the boundaries, as illustrated in Fig. 9 for the system with  $\lambda_0 = 4.88$  and  $w^R = 2$  mm. Notice that the material is shown in the reference configuration and the color map refers to the magnitude of the vector of the growth velocity,  $V^R$ . Accordingly, in the proportionate

growth stage (which starts at  $t = 46$  h and continues until the end of the simulation), the components perpendicular to the substrate,  $V_{d,3}^R$  and  $V_{a,3}^R$ , are constant for both velocities along the respective boundary, yet the magnitudes of the velocity vectors are not.

By examining the relation for the driving force of growth (14), in view of the boundary conditions on the dissociation surface (i) free boundary ( $\bar{s} = 0$ ) in (5) and (ii) continuity of chemical potential (7), it becomes clear that  $V_d^R(\mathbf{u}, \mu) \approx V_d^R(J)$ . In contrast, at the association surface, the spatial and temporal variations of  $V_a^R$  do not show similar dependence on  $J$  and are negligible when compared to  $V_d^R$ . From our numerical investigation we find that  $V_a^R(\mathbf{u}, \mu) \approx V_a^R(\mu)$ . The swelling ratio  $J$  is shown in Fig. 5 and the chemical potential  $\mu$  is shown in Fig. A1 of the Appendix. Overall, these dependencies elucidate the interplay between morphogenesis and the swelling on the dissociation surface,  $J_d$ : while morphogenesis is the main driver of the time evolution of  $J_d$ , the changes in  $J_d$ , in turn, lead to the slowdown and eventual conclusion of morphogenesis.

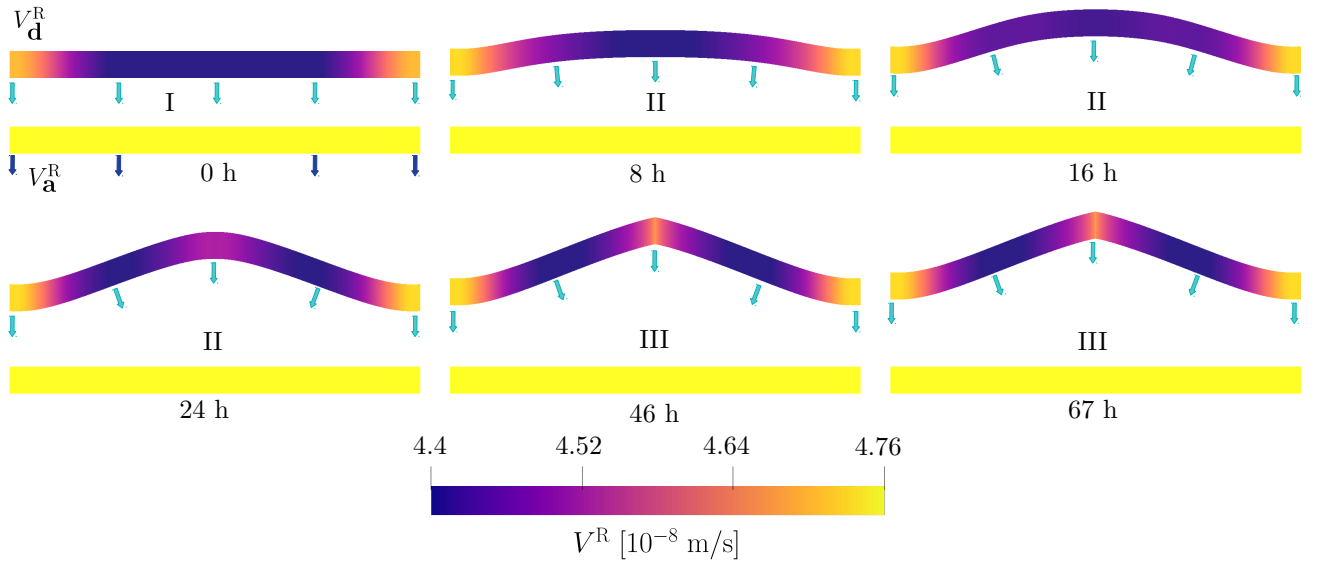


Figure 9: Evolution of the dissociation and association velocity over time in the reference configuration for  $w^R = 2$  mm and  $\lambda_0 = 4.88$ . The boundary normals of the dissociation surface  $\mathbf{n}_d^R$  are denoted by light blue arrows at each time, while  $\mathbf{n}_a^R$  are shown as dark blue arrows only for 0 h and remain constant over time.

### 4.3. Influence of the growth regularization step

The regularization step, presented in Section 3.3, removes residual stresses that may be induced by differential growth along the association surface. Although this assumption becomes accurate for the limits of an infinitely wide association surface (i.e. uniaxial growth) and for a thin association surface (i.e. growth of a filament), it remains to determine its influence on growth of finite layers, as considered in this work.

In the present system, the dry length of material that has been formed at a given point on the substrate, between the time of initiation of growth ( $t = 0$ ) and time  $t$ , is  $\int_0^t V_a^R dt$ . An upper bound estimation of the differential growth can be obtained as

$$\Delta l^R(t) \sim \max \{ \Delta V_a^R \} \cdot t, \quad (36)$$

where,  $\max\{\Delta V_a^R\}$  is taken as the maximum difference in association velocities between two points throughout the growth process. Effects of differential growth are expected to be small if  $\Delta l^R \ll w^R$ , where  $w^R$  is used as a representative distance between the two points.

To estimate the influence of differential growth in our system, for the discussed setting with  $\lambda_0 = 4.907$ , we use the maximum difference in growth rate, which occurs between points A and C of the association surface (points located as illustrated in Figure 8), and we consider the final time of the simulation  $t = 67.5$  h. From the simulation results we find that at point A -  $V_a^R = 4.758 \times 10^{-8} \text{ m s}^{-1}$  and at point C -  $V_a^R = 4.750 \times 10^{-8} \text{ m s}^{-1}$  and thus,  $\Delta V_a^R = 8 \times 10^{-11} \text{ m s}^{-1}$ . This difference is found to remain approximately constant through time.

For all of the shown simulations, the width in the reference configuration is of the order of  $w^R \sim 1$  mm, hence the ratio is

$$\Delta l^R / w^R \sim 0.01, \quad (37)$$

Accordingly, in the present setting, the resulting residual stresses can be considered negligible.

Although the above argument cannot capture coupled effects, which in complex growth settings can drive formation of residual stresses through a positive feedback loop, it provides a strong indication that residual stresses have a negligible effect on growth of finite layers with the considered material properties. Further advancement of the numerical method is required to determine the limits of this assumption and to consider growth on nonuniform substrates.

## 5. Concluding remarks

In this paper, we developed a numerical framework for simulating the evolution of bodies that can grow and dissociate due to chemical reactions that occur on their boundaries. The presented framework captures the coupled effects of large deformations and diffusion on the response in the bulk and on the kinetics that drive the boundary reactions. Three main ingredients are incorporated to facilitate the numerical integration in both space and time: (i) The coupling between the nonlinear diffusion and deformation fields in the bulk is treated via finite element discretization; it is initiated for given initial body dimensions via a specialized scheme and then solved using an iterative time-marching method consisting of a Newton-Raphson linearization. (ii) The rates of association and dissociation determined by the kinetic relation are used to determine the evolution of the integration domain and simplified via a volume preserving regularization step, which is shown to provide accurate results in the considered material system. (iii) The new domain is updated explicitly and remeshed upon convergence of the Newton-Raphson iterations at every time step. Upon validation of the numerical framework in comparison with analytical results obtained for a uniaxial growth setting, we present simulations of growth of finite bodies in a generalized plane-strain setting and exam sensitivities of the growth process to properties of the association surface. From these simulations, four distinct stages of growth emerge; a rapid diffusion-dominated stage is followed by a morphogenesis stage, then a proportionate growth stage appears and exhibits minimal changes in shape, until a treading state is attained. These growth stages that spontaneously appear in our simulations which include only the basic mechanisms by which material systems may grow and evolve, exhibit a striking similarity to growth processes that occur in nature, hence these results can potentially help interpret observations of growth. While the present approach is shown to apply for growth of finite bodies on flat uniform substrates, future work should center on extension of this model to arbitrary geometrical settings.

## Appendix

### A.1. Linearization

As described in Section 3.4, the configuration that the iterative procedure is initialized with is non-homogeneous, due to initial swelling subjected to the substrate constraint. To obtain this configuration, a preliminary numerical scheme facilitates convergence by using a linearized version of the constitutive relations, as detailed next. To simplify the momentum balance equation we write the linearized form of (20), using the following Taylor expansion

$$\ln(1-x) = -\sum_{n=0}^{\infty} \frac{1}{n+1} x^{n+1}, \quad (\text{A1})$$

which is valid for  $0 \leq x < 1$ . Then, taking  $x = 1/J$  in (A1) yields

$$\ln\left(1 - \frac{1}{J}\right) = -\frac{1}{J} - \frac{1}{J^2} - \mathcal{O}\left(\frac{1}{J}\right)^3. \quad (\text{A2})$$

Under the assumption that  $J \gg 1$ , higher order terms can be neglected and this finally leads to the expression

$$p = \mu - \mu_0 - \frac{kT}{\nu} \left( \frac{\chi - 0.5}{J^2} \right), \quad (\text{A3})$$

which can then be inserted into equation (18).

To simplify the evaluation of mass balance (6), the reduced form of the flux becomes

$$\mathbf{j}^R = -\frac{D\nu}{kT} \text{Grad}\mu. \quad (\text{A4})$$

Next, we simplify the energy of mixing (17) using (A1), which after dropping higher order terms and inserting the relation  $\phi_R = J - 1$  reads

$$\psi_s(J) = (J-1)\psi_0 + \frac{kT}{\nu} \left( \chi - 1 - \frac{\chi}{J} + \frac{1}{J^2} \right) \quad (\text{A5})$$

which is then inserted into equation (22) as part of the driving force  $f$ .

### A.2. Chemical potential field

Fig. A1 illustrates the evolution of the chemical potential from diffusion to treadmilling. Note that, due to the chemical potential boundary condition (7),  $\mu$  is constant along the dissociation boundary. The transformation of solvent to solid material at the association boundary leads to a reduced chemical potential, with the minimum value occurring at the midpoint. Unlike volume change  $J$ , the chemical potential  $\mu$  does not undergo a significant evolution on the association or dissociation surface once diffusion has equilibrated after 0.5 h.

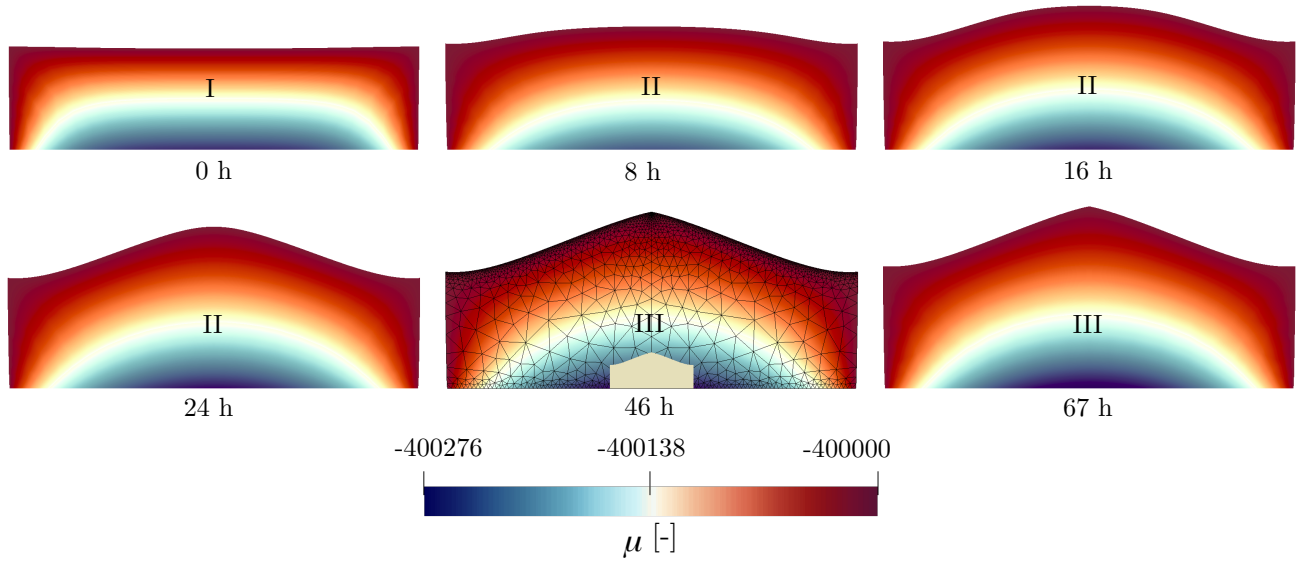


Figure A1: Evolution of the chemical potential for  $w^R = 2$  mm with prestretch  $\lambda_0 = 4.88$  in the current configuration. (I) Diffusion-dominated stage, (II) morphogenesis, (III) proportionate growth.

### A.3. Evolution up to treading

For the sample with  $\lambda_0 = 4.907$  and initial thickness  $l^R = 0.5$  mm, treading is achieved immediately after morphogenesis, thus circumventing the proportionate growth stage.

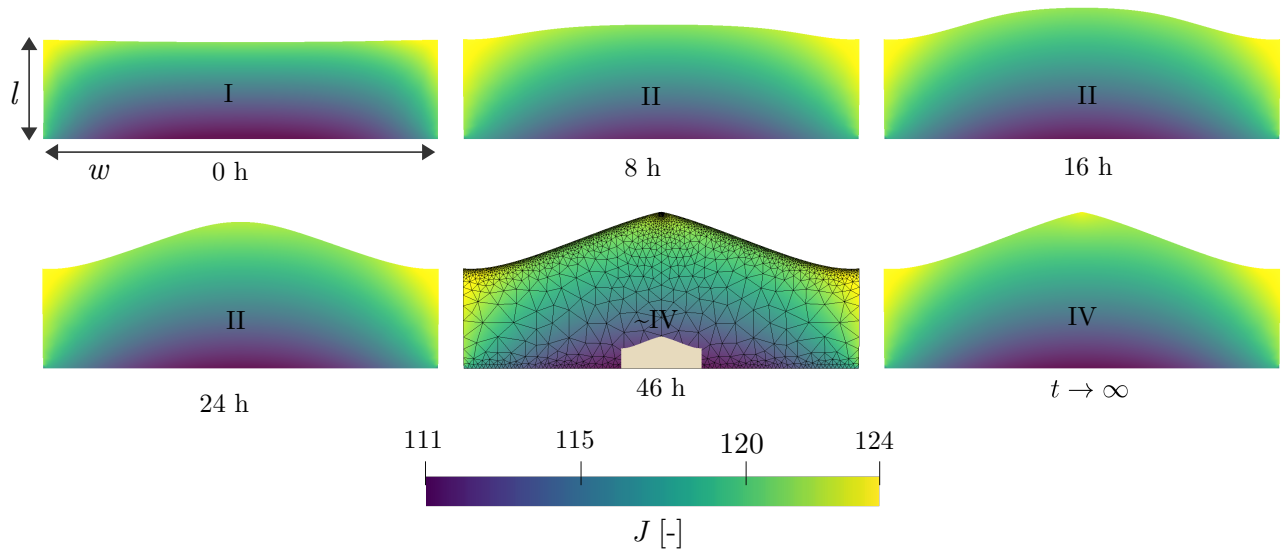


Figure A2: Evolution of the swelling ratio,  $J$  for  $w^R = 2$  mm with prestretch  $\lambda_0 = 4.907$  in the current configuration. Different stages of growth are shown: (I) Diffusion-dominated stage, (II) morphogenesis, and (IV) treading, approached at  $t > 46$  h. The corresponding video is provided in the [supplementary material](#).

## References

- Abeyaratne, R., Puntel, E., Tomassetti, G., 2020. Treadmilling stability of a one-dimensional actin growth model. *International Journal of Solids and Structures* 198, 87–98. doi:10.1016/j.ijsolstr.2020.04.009.
- Abi-Akl, R., Abeyaratne, R., Cohen, T., 2019a. Kinetics of surface growth with coupled diffusion and the emergence of a universal growth path. *Proceedings of the Royal Society A* 475, 20180465. doi:10.1098/rspa.2018.0465.
- Abi-Akl, R., Cohen, T., 2020. Surface growth on a deformable spherical substrate. *Mechanics Research Communications* 103, 103457. doi:10.1016/j.mechrescom.2019.103457.
- Abi-Akl, R., Ledieu, E., Enke, T.N., Cordero, O.X., Cohen, T., 2019b. Physics-based prediction of biopolymer degradation. *Soft Matter* 15, 4098–4108. doi:10.1039/C9SM00262F.
- Ahrens, J., Geveci, B., Law, C., 2005. *Visualization Handbook*. Elsevier. chapter ParaView: An End-User Tool for Large Data Visualization. pp. 717–731.
- Alnæs, M.S., Blechta, J., Hake, J., Johansson, A., Kehlet, B., Logg, A., Richardson, C., Ring, J., Rognes, M.E., Wells, G.N., 2015. The fenics project version 1.5. *Archive of Numerical Software* 3, 9–23. doi:10.11588/ans.2015.100.20553.
- Ateshian, G.A., 2007. On the theory of reactive mixtures for modeling biological growth. *Biomechanics and modeling in mechanobiology* 6, 423–445. doi:10.1007/s10237-006-0070-x.
- Bischofberger, I., Nagel, S.R., 2016. Fluid instabilities that mimic animal growth. *Physics today* 69, 70–71. doi:10.1063/PT.3.3307.
- Budday, S., Steinmann, P., Kuhl, E., 2014. The role of mechanics during brain development. *Journal of the Mechanics and Physics of Solids* 72, 75–92. doi:10.1016/j.jmps.2014.07.010.
- Chester, S.A., Anand, L., 2010. A coupled theory of fluid permeation and large deformations for elastomeric materials. *Journal of the Mechanics and Physics of Solids* 58, 1879–1906. doi:10.1016/j.jmps.2010.07.020.
- Chester, S.A., Di Leo, C.V., Anand, L., 2015. A finite element implementation of a coupled diffusion-deformation theory for elastomeric gels. *International Journal of Solids and Structures* 52, 1–18. doi:10.1016/j.ijsolstr.2014.08.015.
- Ciarletta, P., Preziosi, L., Maugin, G., 2013. Mechanobiology of interfacial growth. *Journal of the Mechanics and Physics of Solids* 61, 852–872. doi:10.1016/j.jmps.2012.10.011.
- Cordero, O.X., Stocker, R., 2017. A particularly useful system to study the ecology of microbes. *Environmental microbiology reports* 9, 16–17.
- Cross, M.C., Hohenberg, P.C., 1993. Pattern formation outside of equilibrium. *Reviews of modern physics* 65, 851.

- DiCarlo, A., 2005. Surface and bulk growth unified, in: *Mechanics of material forces*. Springer, Boston, MA, pp. 53–64. doi:10.1007/0-387-26261-X\_6.
- Duda, F.P., Souza, A.C., Fried, E., 2010. A theory for species migration in a finitely strained solid with application to polymer network swelling. *Journal of the Mechanics and Physics of Solids* 58, 515–529. doi:10.1016/j.jmps.2010.01.009.
- Feynman, R.P., Leighton, R.B., Sands, M., 1963. *The Feynman Lectures on Physics*, vol. I. Addison-Wesley, Reading, MA.
- Flory, P.J., 1942. Thermodynamics of high polymer solutions. *The Journal of chemical physics* 10, 51–61. doi:10.1063/1.1723621.
- Flory, P.J., Rehner, J.J., 1943. Statistical mechanics of cross-linked polymer networks ii. swelling. *The Journal of Chemical Physics* 11, 521–526. doi:10.1063/1.1723792.
- Ganghoffer, J.F., Goda, I., 2018. A combined accretion and surface growth model in the framework of irreversible thermodynamics. *International Journal of Engineering Science* 127, 53–79. doi:10.1016/j.ijengsci.2018.02.006.
- Geuzaine, C., Remacle, J.F., 2009. Gmsh: A 3-D finite element mesh generator with built-in pre- and post-processing facilities. *International Journal for Numerical Methods in Engineering* 79, 1309–1331. doi:10.1002/nme.2579.
- Goli, E., Robertson, I.D., Agarwal, H., Pruitt, E.L., Grolman, J.M., Geubelle, P.H., Moore, J.S., 2019. Frontal polymerization accelerated by continuous conductive elements. *Journal of Applied Polymer Science* 136, 47418.
- Holland, M.A., Kosmata, T., Goriely, A., Kuhl, E., 2013. On the mechanics of thin films and growing surfaces. *Mathematics and Mechanics of Solids* 18, 561–575. doi:10.1177/1081286513485776.
- Hong, W., Zhao, X., Zhou, J., Suo, Z., 2008. A theory of coupled diffusion and large deformation in polymeric gels. *Journal of the Mechanics and Physics of Solids* 56, 1779–1793.
- Horstmann, B., Single, F., Latz, A., 2018. Review on multi-scale models of solid-electrolyte interphase formation. *Current Opinion in Electrochemistry* .
- Johnson, R.L., Tabin, C.J., 1997. Molecular models for vertebrate limb development. *Cell* 90, 979–990.
- Lai, Y., Hu, Y., 2018. Probing the swelling-dependent mechanical and transport properties of polyacrylamide hydrogels through afm-based dynamic nanoindentation. *Soft matter* 14, 2619–2627. doi:10.1039/C7SM02351K.
- Li, J., Mooney, D.J., 2016. Designing hydrogels for controlled drug delivery. *Nature Reviews Materials* 1, 16071.
- Liu, Y., Yang, X., Cao, Y., Wang, Z., Chen, B., Zhang, J., Zhang, H., 2015a. Dehydration of core/shell fruits. *Computers & Graphics* 47, 68–77.



- Liu, Y., Zhang, H., Zheng, Y., 2015b. A multiplicative finite element algorithm for the inhomogeneous swelling of polymeric gels. *Computer Methods in Applied Mechanics and Engineering* 283, 517–550.
- Logg, A., Mardal, K.A., Wells, G.N., et al., 2012. *Automated Solution of Differential Equations by the Finite Element Method*. Springer. doi:10.1007/978-3-642-23099-8.
- Lucas, T., Waisman, A., Ranjan, R., Roes, J., Krieg, T., Müller, W., Roers, A., Eming, S.A., 2010. Differential roles of macrophages in diverse phases of skin repair. *The Journal of Immunology* 184, 3964–3977.
- Menzel, A., Kuhl, E., 2012. Frontiers in growth and remodeling. *Mechanics research communications* 42, 1–14. doi:10.1016/j.mechrescom.2012.02.007.
- Metzger, R.J., Krasnow, M.A., 1999. Genetic control of branching morphogenesis. *science* 284, 1635–1639.
- Mogilner, A., Oster, G., 1996. Cell motility driven by actin polymerization. *Biophysical journal* 71, 3030–3045. doi:10.1016/S0006-3495(96)79496-1.
- Mogilner, A., Oster, G., 2003. Force generation by actin polymerization ii: the elastic ratchet and tethered filaments. *Biophysical journal* 84, 1591–1605. doi:10.1016/S0006-3495(03)74969-8.
- Moulton, D.E., Goriely, A., Chirat, R., 2012. Mechanical growth and morphogenesis of seashells. *Journal of theoretical biology* 311, 69–79. doi:10.1016/j.jtbi.2012.07.009.
- Noireaux, V., Golsteyn, R., Friederich, E., Prost, J., Antony, C., Louvard, D., Sykes, C., 2000. Growing an actin gel on spherical surfaces. *Biophysical journal* 78, 1643–1654. doi:10.1016/S0006-3495(00)76716-6.
- Papastavrou, A., Steinmann, P., Kuhl, E., 2013a. On the mechanics of continua with boundary energies and growing surfaces. *Journal of the Mechanics and Physics of Solids* 61, 1446–1463. doi:10.1016/j.jmps.2013.01.007.
- Papastavrou, A., Steinmann, P., Kuhl, E., 2013b. On the mechanics of continua with boundary energies and growing surfaces. *Journal of the Mechanics and Physics of Solids* 61, 1446–1463.
- Robertson, I.D., Yourdkhani, M., Centellas, P.J., Aw, J.E., Ivanoff, D.G., Goli, E., Lloyd, E.M., Dean, L.M., Sottos, N.R., Geubelle, P.H., et al., 2018. Rapid energy-efficient manufacturing of polymers and composites via frontal polymerization. *Nature* 557, 223.
- Sadhu, T., Dhar, D., 2012. Modelling proportionate growth. *Curr. Sci* 103.
- Savin, T., Kurpios, N.A., Shyer, A.E., Florescu, P., Liang, H., Mahadevan, L., Tabin, C.J., 2011. On the growth and form of the gut. *Nature* 476, 57–62.
- Skalak, R., Dasgupta, G., Moss, M., Otten, E., Dullemeijer, P., Vilmann, H., 1982. Analytical description of growth. *Journal of Theoretical Biology* 94, 555–577. doi:10.1016/0022-5193(82)90301-0.

- Skalak, R., Farrow, D., Hoger, A., 1997. Kinematics of surface growth. *Journal of mathematical biology* 35, 869–907. doi:10.1007/s002850050081.
- Slaughter, B.V., Khurshid, S.S., Fisher, O.Z., Khademhosseini, A., Peppas, N.A., 2009. Hydrogels in regenerative medicine. *Advanced materials* 21, 3307–3329.
- Sorg, H., Tilkorn, D.J., Hager, S., Hauser, J., Mirastschijski, U., 2017. Skin wound healing: an update on the current knowledge and concepts. *European Surgical Research* 58, 81–94.
- Sozio, F., Yavari, A., 2017. Nonlinear mechanics of surface growth for cylindrical and spherical elastic bodies. *Journal of the Mechanics and Physics of Solids* 98, 12–48. doi:10.1016/j.jmps.2016.08.012.
- Sozio, F., Yavari, A., 2019. Nonlinear mechanics of accretion. *Journal of Nonlinear Science* 29, 1813–1863. doi:10.1007/s00332-019-09531-w.
- Stracuzzi, A., Mazza, E., Ehret, A.E., 2018. Chemomechanical models for soft tissues based on the reconciliation of porous media and swelling polymer theories. *Journal of Applied Mathematics and Mechanics* 98, 2135–2154. doi:10.1002/zamm.201700344.
- Swain, D., Gupta, A., 2018. Biological growth in bodies with incoherent interfaces. *Proceedings of the Royal Society A: Mathematical, Physical and Engineering Sciences* 474, 20170716.
- Tallinen, T., Chung, J.Y., Rousseau, F., Girard, N., Lefèvre, J., Mahadevan, L., 2016. On the growth and form of cortical convolutions. *Nature Physics* 12, 588–593.
- Thompson, D.W., 1917. *On growth and form*. University Press, Cambridge [Eng.].
- Tomassetti, G., Cohen, T., Abeyaratne, R., 2016. Steady accretion of an elastic body on a hard spherical surface and the notion of a four-dimensional reference space. *Journal of the Mechanics and Physics of Solids* 96, 333–352. doi:10.1016/j.jmps.2016.05.015.
- Truster, T.J., Masud, A., 2017. A unified mixture formulation for density and volumetric growth of multi-constituent solids in tissue engineering. *Computer Methods in Applied Mechanics and Engineering* 314, 222–268. doi:10.1016/j.cma.2016.09.023.
- Turing, A.M., 1952. The chemical basis of morphogenesis. *Philosophical Transactions of the Royal Society of London. Series B, Biological Sciences* 237, 37–72. doi:10.1098/rstb.1952.0012.
- Wang, J., Zhang, H., Zheng, Y., Ye, H., 2020. High-order nurbs elements based isogeometric formulation for swellable soft materials. *Computer Methods in Applied Mechanics and Engineering* 363, 112901. doi:10.1016/j.cma.2020.112901.
- Zurlo, G., Truskinovsky, L., 2017. Printing non-euclidean solids. *Phys. Rev. Lett.* 119, 048001. doi:10.1103/PhysRevLett.119.048001.
- Zurlo, G., Truskinovsky, L., 2018. Inelastic surface growth. *Mechanics Research Communications* 93, 174–179. doi:10.1016/j.mechrescom.2018.01.007.